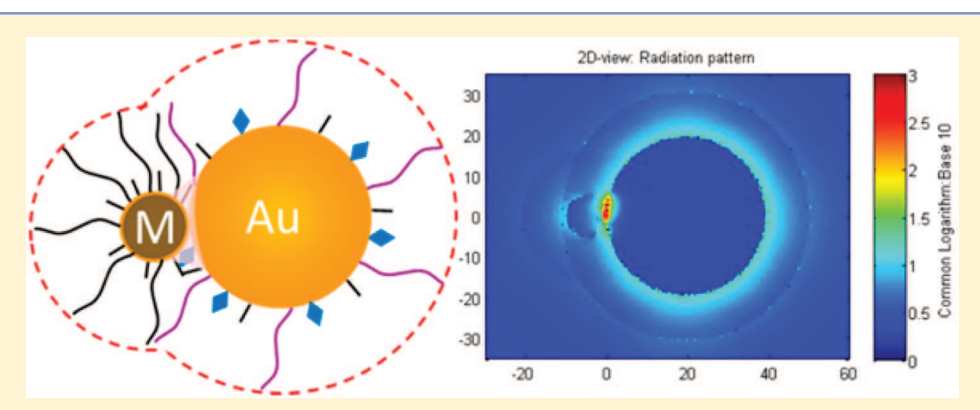
Assessing Interparticle Spatial Characteristics of DNA-Linked Core— Shell Nanoparticles with or without Magnetic Cores in Surface **Enhanced Raman Scattering**

Zakiya Skeete, Han-Wen Cheng,[†] Jing Li, Christian Salazar, Winny Sun, Quang Minh Ngo,[‡] Liqin Lin, Jin Luo, and Chuan-Jian Zhong*

Department of Chemistry, State University of New York at Binghamton, Binghamton, New York 13902, United States

Supporting Information



ABSTRACT: Surface-enhanced Raman scattering (SERS) of plasmonic nanoparticles enables their use as nanoprobes for the detection of biomolecules in solutions, which exploits the "hot-spot" arisen from small aggregates of the biomolecule-linked nanoprobes for effective harnessing of the interparticle plasmonic coupling of gold nanoparticles. While a "squeezed" interparticle spatial characteristic has been revealed from the duplex DNA-linked gold nanoparticles as dimers in solution, how this interparticle spatial characteristic is operative for plasmonic nanoparticles containing magnetic components remains unknown. We describe herein new findings of an investigation of the interparticle spatial characteristics of DNA-linked core-shell type nanoparticles consisting of magnetic cores and plasmonic gold or silver shells, focusing on theoretical-experimental correlation in terms of localized surface plasmon resonance and electromagnetic field enhancement. While the simulated enhancement for the DNA-linked dimers of plasmonic magnetic core-gold shell nanoprobes shows an agreement with the experimental data in terms of the squeezed interparticle spacing characteristic, it does not seem to show an agreement between the simulated and experimental results for the dimers involving magnetic core-silver shell nanoprobes. Instead, an agreement was revealed by simulations of the DNA-linked dimers of the nanoprobes at an interparticle spacing of essentially zero. This finding was analyzed in terms of effective thickness of DNA layers on the nanoparticles and the strong magnetic attraction for the core-shell nanoprobes, providing new insight into the control of core composition and shell structure in optimizing the plasmonic coupling and spectroscopic enhancements for SERS-based biomolecular detection.

INTRODUCTION

Surface-enhanced Raman scattering (SERS) based theranostics is a rapidly developing field, which allows for rapid and pointof-care detection in medical diagnoses. 1-4 A focal point of interest is the detection of biomolecules in solutions. 1-5 The use of magnetic nanoparticles (MNPs) in such systems allows for the navigation of the biomolecules to desired locations using magnetic fields. The coupling of MNPs with plasmonic effect provides an efficient pathway for biomolecular detection.^{6–11} For instance, Fe₃O₄@Ag and Au@Ag nanorods were used for the capture of protein biomarkers for SERS detection.⁶ Ag-Fe₃O₄ nanocomposites were also studied for producing a positive effect on the plasmonic coupling by controlling the arrangement of the nanocomposites on the substrate. Because

MNPs are composed of metals that are not typically biocompatible and have limited surface chemistry, the functionalization of their surfaces with gold and silver has become an important pathway to the desired surface chemistry. The application of the functionalized nanoparticles (NPs) in biomolecular detection explores the magnetic susceptibility of MNPs in combination with the plasmonic properties of metallic NPs, providing promising opportunities for developing theranostic tools for the early detection and treatment of diseases.^{9,10}

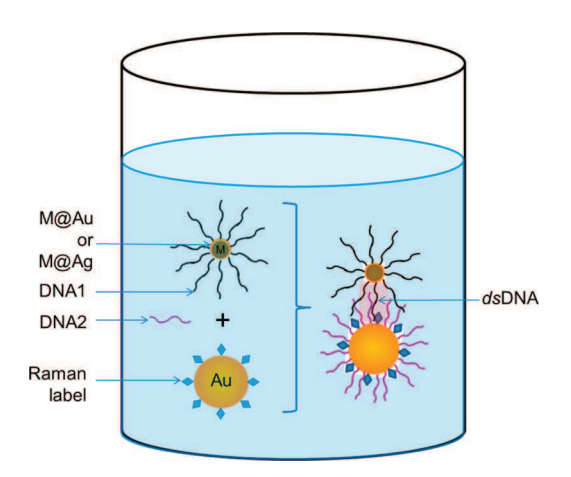
Received: April 26, 2017 Revised: June 30, 2017 Published: July 18, 2017



We have recently reported the interparticle plasmonic coupling responsible for SERS signal amplification as a result of formation of interparticle duplex DNA with gold nanoparticles, revealing a "squeezed" interparticle spatial characteristic in which the duplex DNA-defined distance is shorter than A-form DNA conformation. 12 Similar studies were also reported, including the analysis of Au-Ag nanodimers that demonstrated a stronger SERS intensity at a lower interparticle distance than expected, ^{13–16} and the enhanced NP coupling with magnetic particles due to dipolar interactions in addition to the axis orientation. ^{17,18} Despite these studies, how this type of interparticle interaction is operative for plasmonic nanoparticles containing magnetic component remains unclear. Recent studies have employed simulation methods and SOUID technique to address this issue. 7,19 For example, Fan et al. showed that the SERS intensity of Ag-Fe₃O₄ nanocomposites was dependent on the external magnetic field and the gap distance between Ag and Fe₃O₄ NPs. Similarly, Srivastava et al. analyzed the assembly of FePt or Au NPs with ferritin using SQUID technique and found that the magnetic core of the protein increased the magnetic interaction of the nanoparticles. 19 There were also studies 12,20,21 using TEM techniques to address interparticle spatial properties, which were complicated by sample-drying induced aggregation (see Supporting Information Figure S1 as an example). Although there have been extensive interests in applications of magnetic and plasmonic nanocomposites, there is limited understanding of how the magnetic core of the NP plays a role in the "hotspot" formation for SERS detection of biomolecules. In an earlier report,⁸ we demonstrated that magnetic MnZn ferrite NPs decorated with Au or Ag atoms or shells on the surface (M@Au or M@Ag) functioned as effective nanoprobes for SERS detection of double-strand DNA (dsDNA)-linked M@ Au or M@Ag NPs and AuNPs. The experimental data, along with those with interparticle dsDNA-linked AuNPs,² indicated that the SERS intensity depends on the nanoparticle size and composition. However, little is understood on how such a dependence correlates with their interparticle spatial and plasmonic properties.

In this report, the interparticle spatial characteristics of dsDNA-linked core—shell nanoparticles, consisting of magnetic cores and gold or silver shells, and the formation of the SERS hot-spot in solution phase, ⁸ (Scheme 1) are theoretically

Scheme 1. Illustration of Hot-Spot Formation of dsDNA-Linked Core-Shell Nanoparticles Containing Magnetic Cores and Gold (or Silver) Shell in a Solution



modeled using dimers of various combinations of magnetic core—gold or silver shell nanoparticles. The study focuses on the correlation between the experimental SERS data and the theoretical simulations in comparison with those for gold or silver nanoparticle counterparts without magnetic cores, as a control. New insights are gained into how the effective thickness of DNA layers on the nanoparticles and the interparticle interactions for magnetic core—metal shell nanoparticles operate in terms of composition and structure for optimizing the plasmonic coupling and spectroscopic enhancements

EXPERIMENTAL SECTION

Chemicals and Materials. Chemicals used for nanoparticle synthesis and functionalization were sodium citrate (99%), sodium acrylate (97%), silver nitrate (AgNO₃, >99%), hydrogen tetrachloroaurate (III) hydrate (HAuCl₄), sodium borohydride (NaBH₄, 99%), dithiothreitol (DTT), 11mercaptoundecanoic acid (MUA), and 4-mercaptobenzoic acid (MBA), which were used as purchased from Sigma-Aldrich (Milwaukee, WI). Buffers of carbonate/borate (0.05 M, pH 10) and phosphate (0.05 M, pH 7) were purchased from Fisher Scientific (Pittsburgh, PA). Thiol-modified DNA with standard desalting purification for DNA functionalization were purchased from Integrated DNA Technologies, Inc. (Coralville, IA). DNA were purified with 10× TBE (0.89 M Tris, 0.89 M boric acid, 20 mM EDTA) buffer and precast polyacrylamide gels purchased from Biorad Corporation (Hercules, CA). A Millipore Milli-Q water system was used to purify the water $(18.2 \text{ M}\Omega).$

Nanoparticle Synthesis. As reported previously, ^{19–24} citrate-capped gold nanoparticles (11.7 nm) and acrylate-capped gold nanoparticles (39.7 and 62.4 nm) were synthesized. Citrate-capped (10 nm) silver nanoparticles were also synthesized. ^{23,24} The Au- or Ag-coated MnZn ferrite (MZF) nanoparticles (8 nm MZF NP, 9 nm M@Ag NP, and 11 nm M@Au NP) were synthesized using the previously reported procedure and capped with MUA.⁸

DNA-Linked Assemblies of Au or Ag and Core@shell NPs. Two oligonucleotides, 5'-/5ThioMC6-D/AGG-CCAGACCTGCCCGGGCAAGCCTTGGCA-3' (bottom-DNA) and top-DNA: 5'-/5ThioMC6-D/TGCCAAGGCT-TGCCCGGGCAGGTCTGGCCT-3' (top-DNA), were dissolved in 0.1 M phosphate buffer (pH 8) at a concentration ranging from 260 to 300 μ M. The bottom-DNA (10 μ M) was conjugated to acrylate-capped NPs of Au and Ag and MUA-capped MZF NPs. 8,21,24 The labeling of AuNPs with Raman Label (RL), that is, MBA, was achieved similarly to the reported procedure. 8,21,24

Spectroscopic Measurements. The surface plasmon resonance spectra for the assembly of the DNA-conjugated and RL-labeled AuNPs were monitored using Hewlett-Packard (HP) 8453 UV-vis spectrophotometer. The SERS were obtained using DeltaNu Advantage 200A (laser power, 5 mW, and wavelength, 633 nm HeNe laser) spectrometer.

Simulation Method. The electrical intensity of the localized surface plasmon resonances of the NPs were simulated using the MNPBEM toolbox to obtain the absorption and enhancement (log base 10) of the NPs when in an aqueous environment. The MNPBEM toolbox utilizes the optical constants and Maxwell equations to determine the surface charge and currents of the particles.

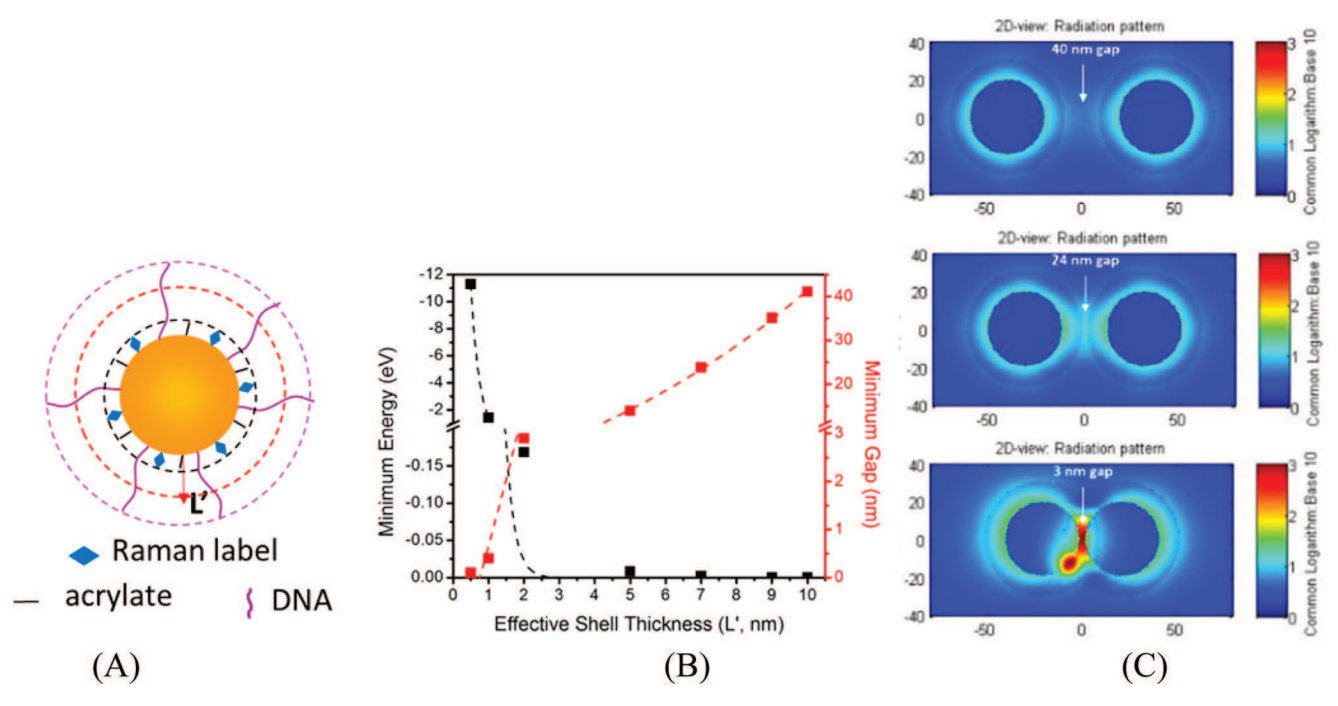


Figure 1. (A,B) Dependencies of the minimum interparticle gap and total interaction energy $(E_{\rm M})$ on effective DNA shell thickness (L') for a dimer of 40 nm NPs (Hamaker constant, 0.82 eV; DNA monolayer thickness, 2 nm; length, 11 nm). (Dashed lines: $E_{\rm min.} = -19.1 \times \exp(-1.6 \times L')$; $G_{\rm min.} = 19.9 \times \exp(0.1 \times L')$). (C) Simulated EMF spectra for dimers of 39 nm AuNP dimers at L' = 10 nm (gap ≈ 40 nm), 7 nm (gap ≈ 24 nm), and 2 nm (gap ≈ 3 nm).

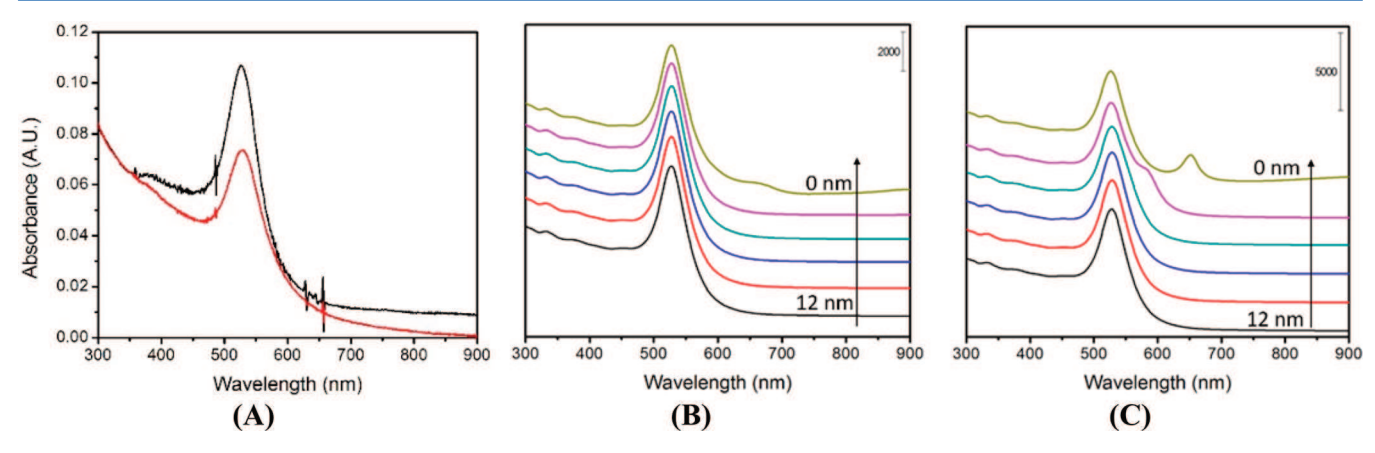


Figure 2. (A) UV-vis spectra for an aqueous solution of MZF@Au-DNA1 and MBA-Au NPs before (black) and after (red) adding DNA2. [MZF@Au-DNA1] = 6.2 nM; [DNA2] = 0.56 μ M; [40 nm-Au@MBA] = 4.3 × 10⁻² nM. (B,C) Simulated ACS spectra of AuNPs assembled to M@Au NPs (B) and AuNPs (C) with different gap distances (12, 7, 6, 2, 1, 0 nm).

■ RESULTS AND DISCUSSION

In our recent study,¹² the interparticle gap of DNA-mediated assembly of AuNPs would subject a small "squeezing" in the presence of AuNPs. However, the role of the DNA or capping ligands in the interparticle interactions remained elusive. Experimentally, for adsorption of surface species into the capping shell structure on the NP surfaces via place exchange reaction,²⁵ the degree of the original capping ligands being replaced by the incoming ligands depends on the competitive adsorption. Thus, there is an effective shell thickness determined by the original and incoming ligands which can impact the interparticle interaction energy, leading to different interaction potentials for different effective shell thicknesses (Figure 1A, and Supporting Information). Figure 1A,B illustrates the changes in terms of the minimum energy and interparticle gap for a dimer of 40 nm AuNPs when the

effective shell thickness (L') of DNA shell is varied from 0.1 to 10 nm, that is, from the original monolayer of citrate (or acrylate) capping to a full monolayer of DNA coverage.

In this case, the effective ligand thickness would be smaller than the expected 11 nm DNA shell length as a result of squeezing in the presence of AuNPs. On the basis of the calculated potentials (Figure S2), under several effective thicknesses (L'=10 nm (gap ≈ 40 nm), 7 nm (gap ≈ 24 nm), and 2 nm (gap ≈ 3 nm)) the simulated EMF intensity at the center of the dimer showed a sharp contrast between L'=10 and 2 nm (Figure 1C). While the center EMF intensity for L'=2 nm displays a clear enhancement, there is essentially no enhancement for L'=10 nm (Figure 1C).

The center EMF intensity for $L^\prime=7$ nm displays an enhancement that is almost the same as that surrounding the NPs. This finding is significant, demonstrating a clear need to

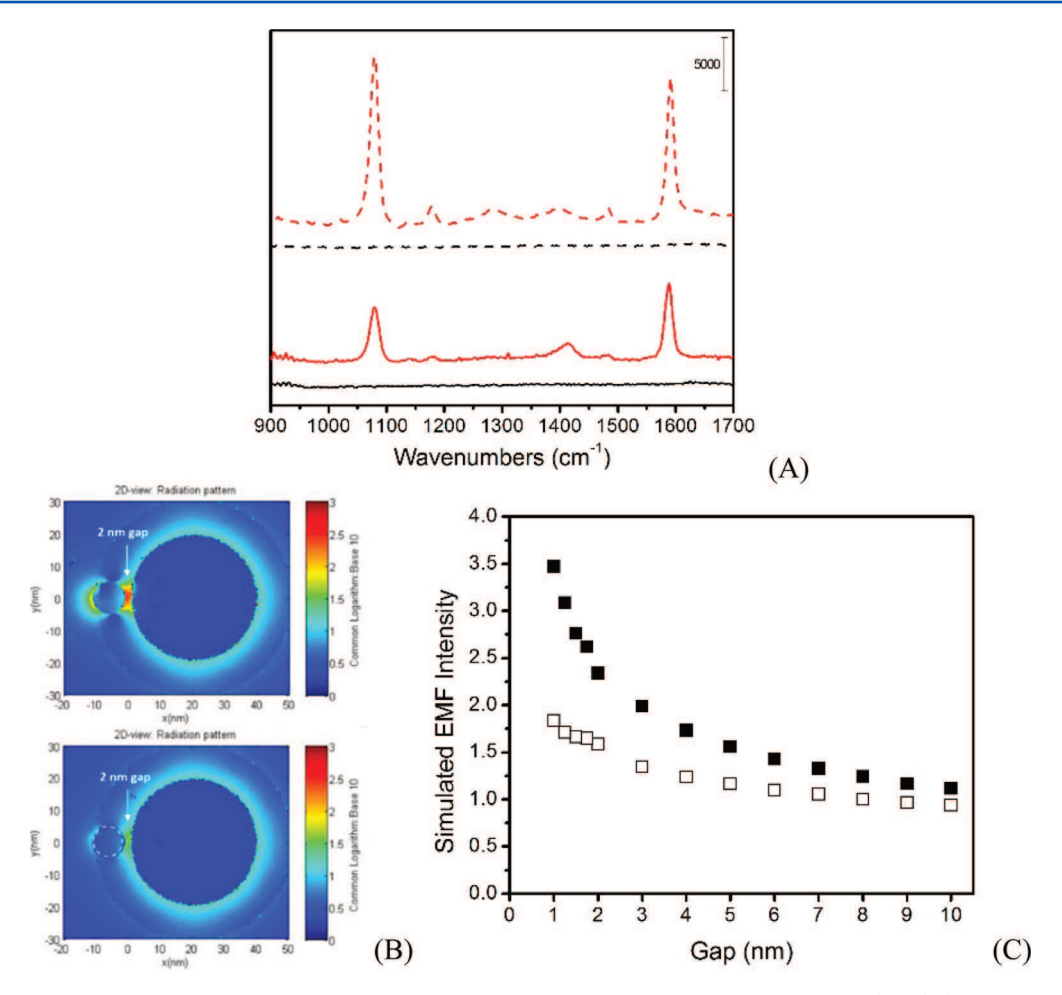


Figure 3. (A) SERS spectra for the assembly of MBA labeled Au NPs and DNA functionalized M@Au NPs (solid) (and AuNPs (dashed)) with target DNA strands (before assembly, black; after assembly, red). (B) A 2D image of the simulated EMF around the Au-M@Au NPs (bottom, 9 nm magnetic core and 0.5 nm Au shell for M@Au NP) and Au-Au NPs (top, 40 nm) at g = 2 nm. (C) Plot of the simulated EMF intensity for the Au-M@Au NPs (open squares) and Au-Au NPs (closed squares) as a function of the interparticle gap (from 1 to 10 nm).

assess the interparticle plasmonic coupling and SERS characteristics in terms of the effective thickness. Similar findings were observed in dimers of smaller (e.g., 13 nm) or larger (e.g., 62 nm) AuNPs (Figure S3). In view of the likelihood that part of the DNA strands are laying down on the surface of the NPs or over the original capping molecules, leading to a significantly squeezed interparticle distance. Our study focused on understanding how such smaller interparticle distance correlates with the interparticle plasmonic coupling and the SERS hot-spot effect, especially for nanoparticles with magnetic cores that could further squeeze the interparticle gap distance (g). The results are discussed in the next few subsections on interparticle plasmonic coupling and electric field enhancement for two different combinations of NPs linked by DNA strands, that is, Au-M@Au NPs and Au-M@Ag NPs. In our recent report, the core-shell structures for M@Au and M@Ag (M = MZF) were characterized using HAADF-STEM imaging and EDS elemental mapping, which revealed the decoration of the MZF NPs with Au or Ag atoms or layers (see Figure S4).

1. Combination of Au–M@Au NPs. In this section, we describe the DNA-mediated assembly of AuNPs and M@Au NPs, that is, Au–M@Au assembly. First, we describe the surface plasmon resonance (SPR) optical characteristics based on experimental UV–vis data and theoretical simulation of the plasmonic coupling. It is then followed by the discussion of the

SERS intensity in correlation with the theoretical simulation of the interparticle electrical field enhancement.

Experimentally, a subtle change can be detected in the SP band as shown by the UV-vis spectra for an aqueous solution of MZF@Au-DNA1 and MBA-Au NPs before and after adding DNA2 (Figure 2A). This change is reflected by a very small red shift in the SP band.

Theoretically, the SP band characteristics of the Au–M@Au NPs were simulated in terms of absorbance cross-section spectra (ACS) as a function of g (Figure 2B). The general feature for the simulated ACS is similar to those observed experimentally. There is no obvious shift in the SP band. The core size is 9 nm whereas the Au shell thickness is 0.5 nm for the simulation in the above example. The insignificant shift of the simulated ACS band for the relatively larger-sized magnetic core and the relatively thinner Au shell thickness is further substantiated by simulations performed for M@Au nanoparticles with different shell thicknesses of gold and different magnetic core sizes (see Supporting Information, Figures S6 and S7).

In comparison with the band characteristics of the Au–M@ Au NPs, the simulated ACS band of Au–Au NPs showed a more redshift as a function of g (Figure 2C). As reflected by the appearance of the longer-wavelength band, the Au–Au NP dimer exhibits a larger shift below 10 nm gap, whereas the band

for the Au-M@Au NP dimer does not show any significant shift until the gap distance is below 5 nm.

An increase in SERS intensity was observed upon the M@Au NPs, as shown by the SERS spectra before and after addition of DNA2 to the solutions of DNA1-M@Au NPs and MBA-Au NPs (Figure 3A). The two major peaks at 1078 and 1592 cm⁻¹ observed in the spectra correspond to the $\nu(CC)$ ring-breathing modes of the Raman label (MBA). In this work, we focused on the 1590 cm⁻¹ peak height as a measure of the SERS intensity.

The SERS intensity of the Raman labels significantly increased upon the addition of the target DNA strands. The SERS intensity was assessed by simulation of the EMF intensity using a dimer model consisting of 10 nm M@AuNP and 40 nm AuNPs as a function of g. Figure 3B shows the 2D images of the simulated EMF around the Au-M@Au NPs (bottom) and Au-Au NPs (top) at g = 2 nm, showing clearly an enhanced intensity at the center of the interparticle gap. The EMF intensity for the Au-M@Au dimer measured at the center of the gap (hot-spot) increases as the interparticle distance increases (Figure 3C, open squares). The EMF intensity for the Au-Au dimer is included for comparison (Figure 3C, closed squares).

It is evident that the EMF intensity for Au-M@Au dimer is smaller than that for Au-Au dimer. A significant increase in EMF at the hot-spot is observed when the gap distance is below 3 nm (Figure 3C). The experimentally observed SERS intensity enhancement is reflected by the theoretically simulated EMF enhancement at the hot-spot.

A comparison of the above experimental data and theoretical simulation results for the Au–M@Au NPs and the Au–Au NPs at g = 2 nm is shown in Figure 4. It is evident that both the

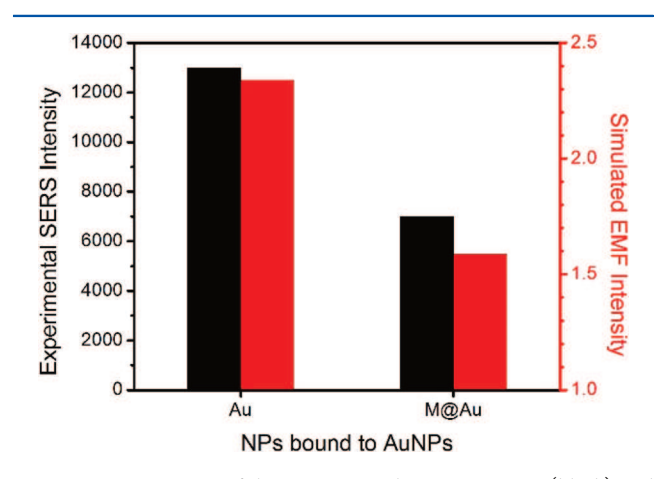


Figure 4. Comparison of the experimental SERS intensity (black) and simulated EMF intensity (red) for the Au-M@Au NPs and the Au-Au NPs at an interparticle gap of 2 nm.

SERS intensity and the EMF intensity for Au-Au NPs are higher than those for the Au-M@Au NPs, showing an excellent agreement between the experimental data and the simulation results. This agreement is also validated for the other interparticle distances. This finding is consistent with the stronger plasmonic coupling for Au-Au NPs than that for the Au-M@Au NPs, as described earlier (see Figure 2B,C).

2. Combination of Au-M@Ag NPs. Using M@Ag NPs to replace M@Au NPs, similar experiments and simulations were performed for the DNA-mediated assembly of AuNPs and M@ Ag NPs, that is, Au-M@Ag assembly. Both the SPR and the

SERS characteristics are discussed in correlation with the theoretical simulation results.

A representative set of UV-vis spectra for the DNAmediated assembly of AuNPs and M@Ag NPs is shown in Figure 5A. In comparison with the spectral features for Au-M@Au (Figure 2A), there appears a stronger plasmonic coupling for the Au-M@Ag, as evidenced by the appearance of the SP band at a longer wavelength (~660 nm), demonstrating a subtle difference in plasmonic coupling between Au-M@Au and Au-M@Ag NPs.

The simulated ACS spectra for Au-M@Ag NPs and the Au-Ag NPs are shown in Figure 5B,C as a function of the interparticle gap. Although there is no significant shift of the main SP band, similar to the case for Au-M@Au NPs and the Au-Au NPs, the spectral feature in terms of the appearance of the longer wavelength band as the interparticle gap approaches zero appears to be in agreement with the UV-vis spectra.

For a further comparison, we also examined the UV-vis spectra for the assembly of AgNPs (10 nm) functionalized with DNA and AuNPs (40 nm) functionalized with MBA (Figure 5A insert). Interestingly, after introduction to the target DNA strand, the appearance of the red-shifted SP band at a longer wavelength (~800 nm) is evident, demonstrating a stronger plasmonic coupling for the Au-Ag NPs than that of Au-Au NPs, and similar intensity in plasmonic coupling between Au-Ag NPs and Au-M@Ag NPs.

A representative set of SERS spectra is shown in Figure 6A for the DNA2 mediated assembly of DNA1-M@Ag NPs and MBA-Au NPs. The SERS for the assembly of Au-Ag NPs is also included for comparison (Figure 6A (dashed lines, top)). There is a clear increase in SERS intensity after the assemblies of both Au-M@Ag and Au-Ag NPs, which was also assessed by simulations. Similar to the simulation for the Au-M@Au NPs and Au-Au NPs, the 2D images of the simulated EMF around the Au-M@Ag NPs and Au-Ag NPs at an interparticle gap of 2 nm also showed a clear enhancement in intensity at the center of the interparticle gap (Figure 6B). The EMF intensity for the Au-M@Ag dimer measured at the center of the gap (hot-spot) increases as the interparticle distance increases (Figure 6C, open circles), which is again lower than that for the Au-Ag dimer (Figure 6C, closed circles). The experimentally observed SERS intensity enhancement is consistent with the trend of the theoretically simulated EMF enhancement at the hot-spot as a function of the interparticle gap.

In Figure 7, the experimental data and theoretical simulation results are compared for Au-M@Ag NPs and Au-Ag NPs at g = 2 nm. In contrast to the trend observed for the Au-M@Au and Au-Au NPs, a discrepancy between the theoretical and experimental data is observed. While the simulated EMF intensity shows a decrease from Au-Ag NPs to Au-M@Ag NPs, the experimental SERS intensity exhibits an opposite trend, the origin of which is discussed in the next subsection.

3. A Comparison between Au-M@Au and Au-M@Ag Combinations. As shown in Figures 4 and 7 for both experimental SERS and simulated EMF at g = 2 nm, there is a clear agreement for the difference between Au-M@Au and Au-Au NPs. However, there is a disagreement for the Au-M@Ag and Au-Ag NPs. Also, the SERS intensity for Au-M@ Ag NPs is higher than that of the Au-M@Au NPs. Note that most experimental observations indicate that silver-based NPs have a stronger SERS enhancement than gold-based NPs. To address the experimental-theoretical disagreement, a key question that must be addressed is how the interparticle

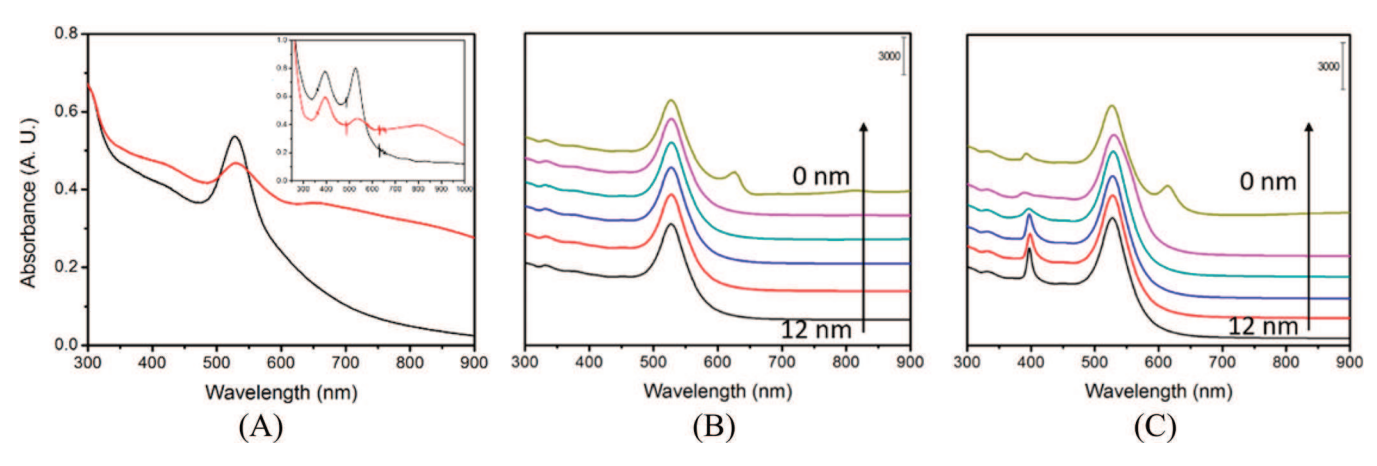


Figure 5. (A) UV–vis spectra for an aqueous solution of MZF@Ag–DNA1 and MBA–AuNPs before (black) and after (red) adding DNA2. Inset in (A) shows before (black) and after (red) assembly of 10 nm Ag NPs and 40 nm Au NPs with DNA. [MZF@Ag-DNA1] = 3.0 nM; [DNA2] = 0.56 μ M; [40 nm-Au@MBA] = 4.3 × 10⁻² nM. (B) The simulated ACS intensity of M@AgNPs and AuNPs when gap distance is decreased from 12 to 0 nm (arrows indicate the trend as the distance decreases: 12, 7, 6, 2, 1, and 0 nm). (C) The simulated EMF intensity of metallic 10 nm AgNPs assembled to 40 nm AuNPs with varying gap distances (arrows show shift from larger to smaller gaps: 12, 7, 6, 2, 1, 0 nm).

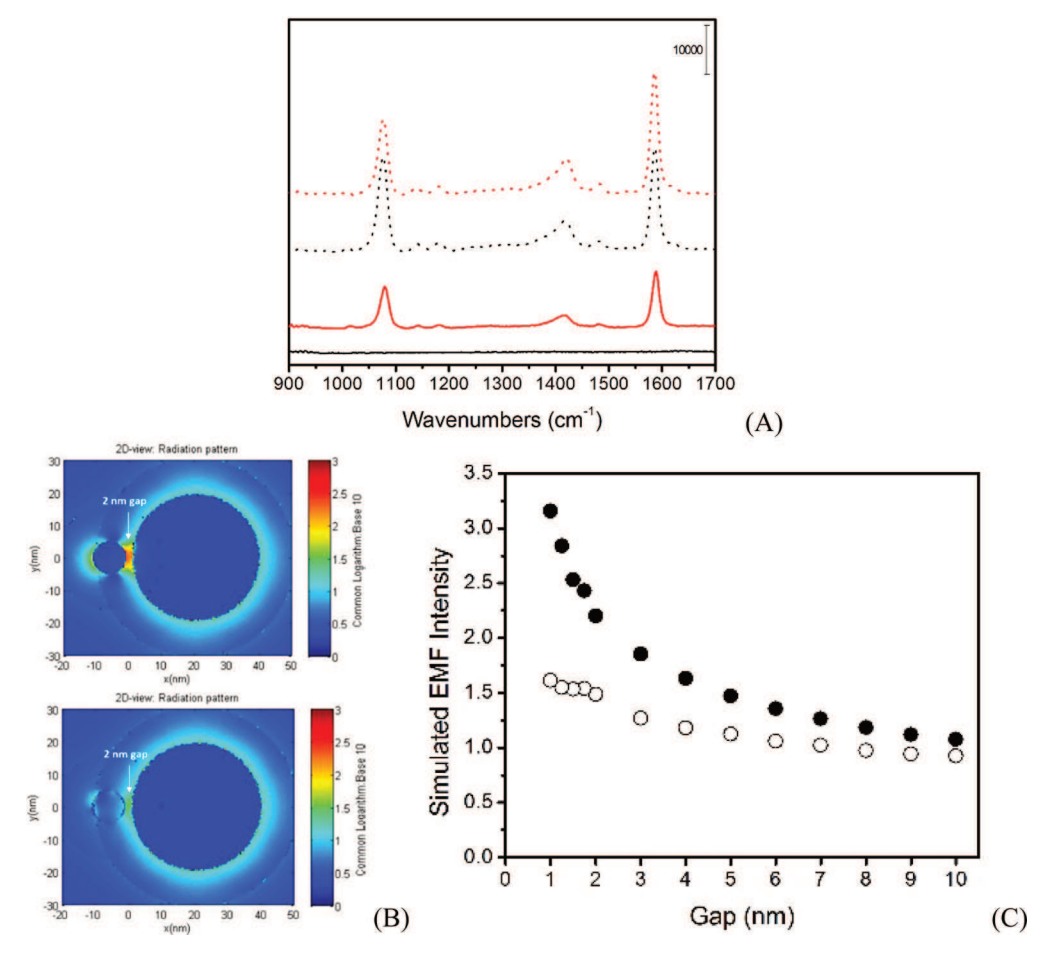


Figure 6. (A) SERS spectrum of Au-M@Ag NPs (top, dotted) and Au-Ag NPs (bottom, solid) before (black) and after (red) assembly. (B) Simulated EMF spectra of the metallic AgNPs assembled to AuNPs (top) and M@AgNPs with AuNPs (bottom) at g=2 nm. (C) The simulated EMF Intensity of 10 nm M@AgNPs (9 nm magnetic core) and AuNPs (open circles) and Ag-Au NP dimers (closed circles) as gap distance decreases from 10 to 1 nm.

spacing is operational for plasmonic coupling of the dimeric nanoparticles in the presence of the magnetic cores and the effective monolayer capping shells.

The interparticle spacing is determined by the interparticle interaction potentials for the DNA-mediated NP assembly,

which were analyzed by considering the monolayer structure in terms of the number of DNA and capping molecules on the NP surface. The approximate number of DNA and other capping molecules on the NP surface can be estimated from the model shown in Figure 1 (see also Supporting Information eqs 3 and

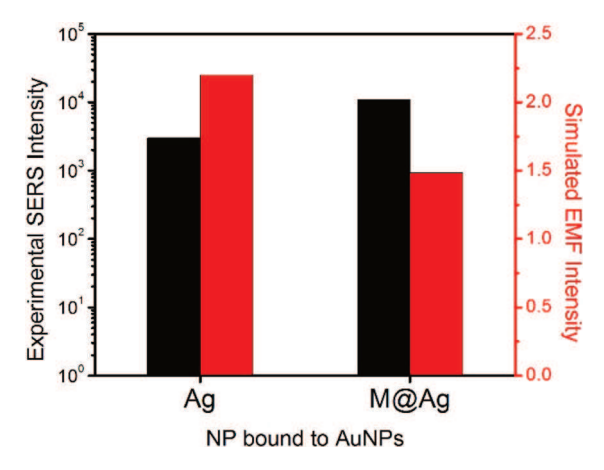


Figure 7. Comparison of the experimental SERS intensity (black) and simulated EMF intensity (red) for the Au–M@Ag NPs and the Au–Ag NPs at an interparticle gap of 2 nm.

4). The estimated effective thickness (L') is dependent on the orientation of DNA strands on the smaller NP surface (Figure 8). When DNA stands on the surface, the thickness is

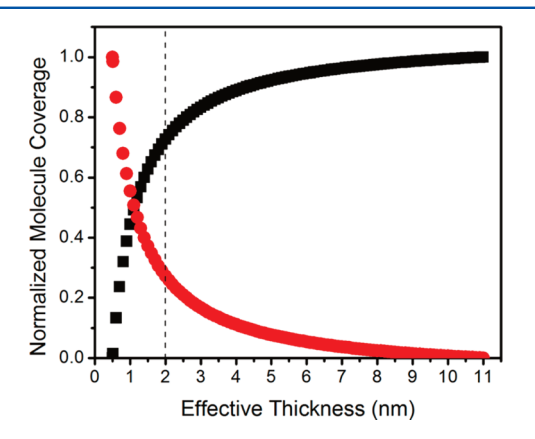


Figure 8. Fractional surface coverage of DNA (black) and acrylate (red) as a function of the effective thickness (L', nm) (DNA, 11 nm height, 2 nm diameter; acrylate, 0.5 nm height, 0.5 nm diameter).

approximately 11 nm, and when laying on the surface it is approximately 2 nm. At an effective thickness of 2 nm, the mixed monolayer consists of 73% DNA. This partial surface coverage provides an explanation of the finding on the small interparticle spacing for the experimental—theoretical correlation (Figures 4 and 7).

We further examined the EMF intensity over the four dimer assemblies for $g \le 2$ nm (Figure 9). Figure 9A shows the simulated EMF spectra of Au–M@Ag at g = 0.1 nm and Figure 9B demonstrates the change in simulated EMF intensity as gap distance decreases from 2 to 0 nm for Au-Au (black, squares) and Au-M@Au (red, circle). As the gap distance decreases, the EMF intensity of Au-Au NP dimers increase to a maximum at 0.5 nm gap and drops thereafter. The Au-M@Au NP dimer shows a similar trend in EMF intensity as the gap decreases and exhibits a maximum at 0.5 nm, except the intensity is much smaller compared to the Au-Au NP dimer. When the NPs come into contact (g = 0 nm), the EMF intensity of the Au-M@Au NPs shows an increase that is practically the same in comparison with that for the Au-Au NP dimer. A similar trend is evident for the EMF intensities observed for Au-Ag and Au-M@Ag NP dimers as the gap drops from 2 to 0 nm

(Figure 9C). A close comparison of this data with the data in Figure 9B, the EMF intensity for the Au–Ag NP dimer showed a less sharp decrease after the maximum at 0.5 nm gap. Interestingly, when gap = 0 nm, the EMF intensity for the Au–M@Ag NP dimers shows a dramatic increase, which is much greater than that for the Au–Ag NP dimer.

The above findings are interesting because the change of the simulated EMF intensities shows sharp contrasts as a function of the interparticle gap. For gap > 0.5 nm, the Au–Au NP dimers display a higher EMF intensity than that of Au–Ag NP dimers. For gap < 0.5 nm, the two systems show similar trends but the intensity of Au–Ag NP dimers is larger than the intensity of Au–Au NP dimers. For dimers of Au–M@Au and Au–M@Ag, apparently, the intensity of Au–M@Au remains higher than Au–M@Ag when gap > 0 nm. However, at gap = 0 nm, the intensity for both Au–M@Au and Au–M@Ag dimers increase sharply although the intensity for Au–M@Ag dimer is greater than that for Au–M@Au dimer.

The simulated results are summarized in Figure 9D,E for an overall comparison with the experimental results. The experimental SERS (red, squares) and simulated EMF (black, circles) intensities are compared for gap > 0 nm and gap = 0nm. For Au-Au and Au-M@Au NP dimers (Figure 9D), the experimental SERS intensity for Au-Au is greater than Au-M@Au dimers, which is consistent with the simulated EMF intensities of Au-Au dimer being greater than Au-M@Au for gap > 0. For g = 0 nm, the EMF for Au–Au is the same as or slightly lower than that of Au-M@Au. For Au-Ag and Au-M@Ag NP dimers (Figure 9E), a sharp contrast is revealed. For gap > 0 nm, the simulated EMF intensity for Au-Ag is higher than that for Au-M@Ag NP dimers. But at g = 0 nm, the simulated EMF intensity for Au-Ag is lower than Au-M@Ag dimer which is clearly consistent with the experimentally observed SERS intensities for Au-Ag dimer being smaller than Au-M@Ag NP dimers.

An important implication from the above results is that the interparticle plasmonic coupling and squeezing are strongly dependent on the composition of the nanoparticles. The presence of Ag and magnetic core in the nanoparticles apparently had a stronger impact on these interparticle properties in comparison with Au. For pure metallic NPs, the effective monolayer thickness falls likely in the range of 1-2nm, whereas the presence of magnetic cores appears to further squeeze the gap distance to approximately 0 nm. Squeezing of the DNA-capped NPs in the interparticle gap favors the peripheral region near the hot-spot contact region (edges of the gap) or in some cases the smaller-sized particle. In these cases, it was found that the highest intensity is not necessarily at the center between the NPs when the gap distance decreases, instead it could be in the peripheral contact region. These assessments were substantiated by a close examination of the EMF in peripheral region (Figure S5) for both Au-M@Au (Figure S5A) and Au–M@Ag (Figure S5B) dimers. They were also substantiated by examining the influence of the relative magnetic core size and metal shell thickness on plasmonic coupling, since M@AuNPs (1.5 nm thick) have a thicker shell than M@AgNPs (0.5 nm thick) used in this experiment (Supporting Information Scheme S1). The simulations were performed in terms of the different relative magnetic core size and metal shell thickness for the NP dimers, including (1) changing magnetic core while keeping the same metal shell thickness (0.5 nm), (2) changing shell thickness while keeping the same core size (9 nm), and (3) changing core size and shell

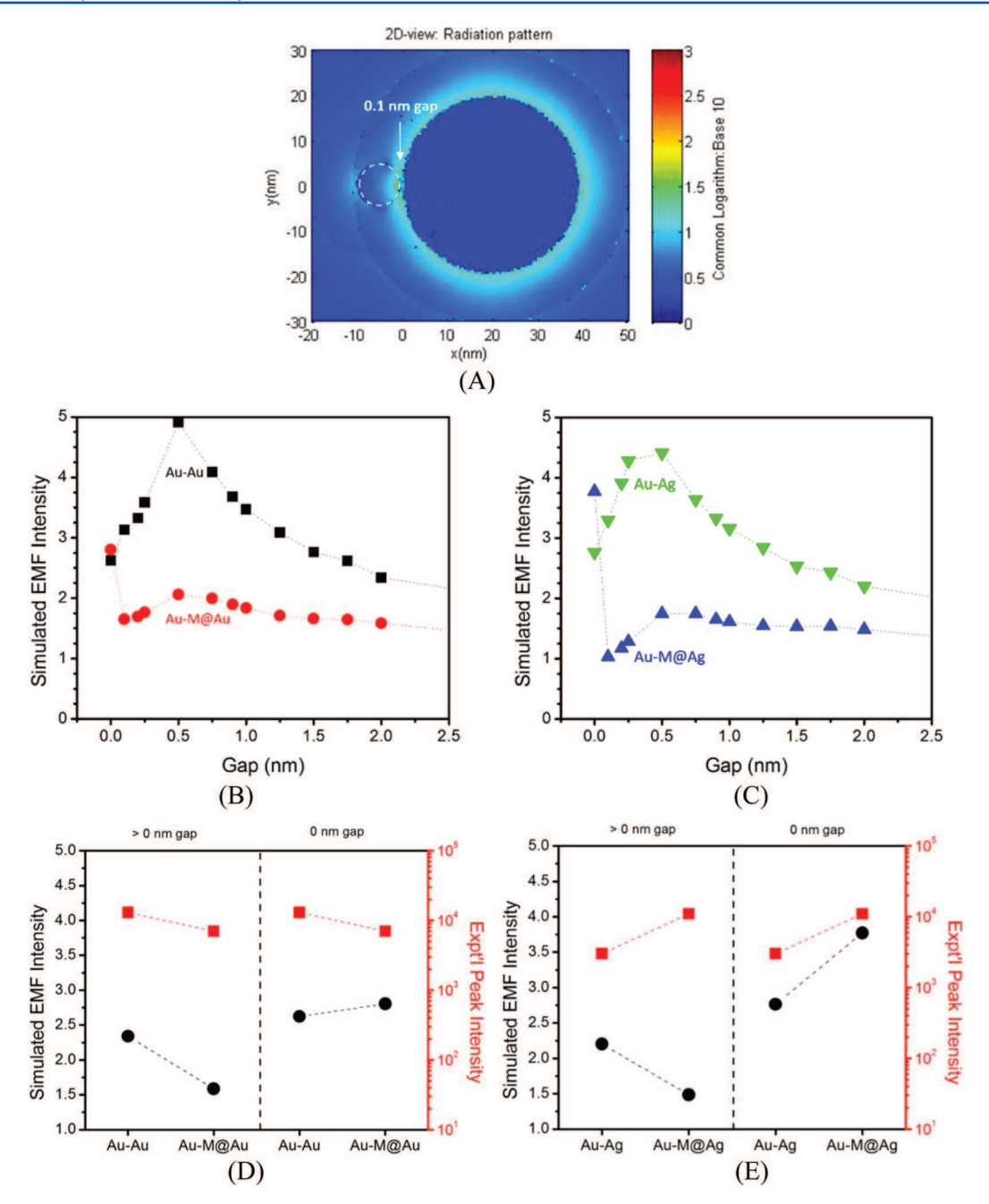


Figure 9. (A) Simulated EMF spectra of Au–M@Ag dimer at 0.1 nm gap. (B,C) Plots of the simulated EMF intensity of 40 nm AuNP and 10 nm NP of Au (black squares), M@Au (red circles) (B), M@Ag (blue up triangles), and Ag (lime downward triangles) (C) at interparticle gaps below 2 nm. (D,E) Comparison of the simulated EMF and SERS intensities for heterodimers of Au–Au based NPs (D) and Au–Ag based NPs (E) above 0 nm (2 nm) and at 0 nm gap distances.

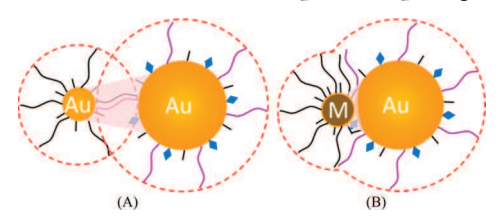
thickness while maintaining the same overall NP size (10 nm). As shown by the SP data (Figures S6 and S7) and the EMF (Figure S7) data, subtle changes in intensities of SP and EMF, as well as the wavelength of SP were observed (Tables S1–S3). Increasing the magnetic core size for Au–M@Au and Au–M@Ag dimers appeared to increase the redshift of the SP band. Similar trends were found when increasing the metal shell thickness of the dimers, except the SP bands initially far-redshifted and slowly shifted back toward the original SP band of the metal. Increasing the shell thickness and magnetic core size for an overall 10 nm sized NP, the SP band showed a slight redshift and decreased intensity. Overall, while the SP band showed slight differences, the Au–M@Ag NP dimer's redshift

was smaller than that for Au–M@Au NP dimer and remained near 700 nm, which is close to the laser's wavelength (633 nm). Similar trends were observed for the EMF intensities upon changing the shell thicknesses for an overall NP size of 10 nm (Figure S8). A maximum EMF intensity was shown at gap = 0.5 nm for all three cases. Increasing the shell thickness leads to an increase in the simulated EMF intensity. These observations are remarkable, suggesting that both the gap and the chemical nature of the materials in the nanoparticles play an important role in the relative strength of interparticle plasmonic coupling.

The metallic NPs appear to exhibit a strong experimentaltheoretical correlation, whereas the correlation for the metalcoated magnetic NPs is apparent only at gap distances below

0.5 nm. It is believed that the magnetic forces could have played an important role in the interparticle interactions other than van der Waals forces. This leads to further squeezing of the interparticle spacing in comparison with only van der Waals interaction, pushing the DNA to the edges of the dimeric contacting point (Scheme 2).

Scheme 2. Illustration of the Interparticle Spacing^a



^ads-NA-linked Au (or Ag)-Au NP dimer (A) and Au-M@Au (or Ag) NP dimer (B) under an effective thickness for the DNA-capped monolayer on the NPs.

Moreover, the NP dimers that involve Ag component appears to have a stronger plasmonic effect than those involving Au component only, even though there appeared to be less Ag on the MNP than Au. This finding could be due to a larger tendency of charge transfer from Ag than Au. 13,14,16 This was further supported by the simulation showing the redshift in SP bands near 700 nm. Experimentally, because the excitation wavelength of the laser is 633 nm, the NP dimers involving Ag components exhibit a higher SERS intensity than those only involving Au components.

CONCLUSION

These results have provided some important new insights into the interparticle spatial characteristics of DNA-linked coreshell type nanoparticles consisting of magnetic cores and plasmonic gold or silver shells in terms of the theoreticalexperimental correlation. In comparison with Au nanoprobes, the simulated results of the SERS enhancement for the DNAlinked dimers of plasmonic-magnetic M@Au nanoprobes show a similar agreement with the experimental data in terms of the squeezed interparticle spacing characteristic. Remarkably, for M@Ag nanoprobes the agreement between the simulated and experimental results for DNA-linked dimers of M@Ag and Au nanoprobes is achieved at an interparticle spacing of essentially zero, implying an important role played by the magnetic interaction in the interparticle interactions. These findings are supported by studies of other core-shell NPs showing significantly reduced interparticle gap distance.¹⁴ These findings also have implications to other systems, including different monolayer shells, different metals (e.g., Cu and alloys), and different magnetic cores (Fe_2O_3 , Fe_3O_4 , and $MnZnFe_2O_4^{~8,26}$, etc.). Part of our ongoing work involves monitoring of the hydrodynamic diameter of dimers or trimers as a result of biomolecule-mediated interparticle aggregation processes.

ASSOCIATED CONTENT

S Supporting Information

The Supporting Information is available free of charge on the ACS Publications website at DOI: 10.1021/acs.jpcc.7b03948.

TEM images, additional calculation or simulation details, and results (Figures S1-S8, Scheme S1, and Tables S1-S3) (PDF)

AUTHOR INFORMATION

Corresponding Author

*E-mail: cjzhong@binghamton.edu.

ORCID

Chuan-Jian Zhong: 0000-0003-0746-250X

Present Addresses

†(H.W.C.) School of Chemical and Environmental Engineering, Shanghai Institute of Technology, Shanghai 201418, China. *(O.M.N.) Institute of Materials Science, Vietnam Academy of Science and Technology, 18 Hoang Quoc Viet Road, Cau Giay, Hanoi, Vietnam.

Notes

The authors declare no competing financial interest.

ACKNOWLEDGMENTS

This work was supported by the National Science Foundation (IIP 164066) and in part by SUNY Research Collaboration Fund. Z.S. also acknowledges the support of the Multidisciplinary GAANN in Smart Energy Materials funded by the U.S. Department of Education (#P200A150135). H.W.C. also acknowledges the support of the Shanghai Sailing Program (16YF1411400).

REFERENCES

- (1) Cheng, H. W.; Luo, J.; Zhong, C. J. SERS Nanoprobes for Bio-Application. Front. Chem. Sci. Eng. 2015, 9, 428-441.
- (2) Jamshaid, T.; Neto, E. T. T.; Eissa, M. M.; Zine, N.; Kunita, M. H.; El-Salhi, A. E.; Elaissari, A. Magnetic Particles: From Preparation to Lab-on-a-Chip, Biosensors, Microsystems and Microfluidics Applications. *TrAC, Trends Anal. Chem.* **2016**, *79*, 344–362.
- (3) De Crozals, G.; Bonnet, R.; Farre, C.; Chaix, C. Nanoparticles with Multiple Properties for Biomedical Applications: A Strategic Guide. Nano Today 2016, 11, 435-463.
- (4) Nam, J.-M.; Oh, J.-W.; Lee, H.; Suh, Y. D. Plasmonic Nanogap-Enhanced Raman Scattering with Nanoparticles. Acc. Chem. Res. 2016, 49, 2746-2755.
- (5) Skeete, Z.; Cheng, H.; Crew, E.; Lin, L.; Zhao, W.; Joseph, P.; Shan, S.; Cronk, H.; Luo, J.; Li, Y.; et al. Design of Functional Nanoparticles and Assemblies for Theranostic Applications. ACS Appl. Mater. Interfaces 2014, 6, 21752-21768.
- (6) Rong, Z.; Wang, C.; Wang, J.; Wang, D.; Xiao, R.; Wang, S. Magnetic Immunoassay for Cancer Biomarker Detection based on Surface-Enhanced Resonance Raman Scattering from Coupled Plasmonic Nanostructures. Biosens. Bioelectron. 2016, 84, 15-21.
- (7) Fan, C.; Zhu, S.; Xin, H.; Tian, Y.; Liang, E. Tunable and Enhanced SERS Activity of Magneto-plasmonic Ag-Fe 3 O 4 Nanocomposites with One Pot Synthesize Method. J. Opt. 2017, 19 (1), 015401.
- (8) Lin, L.; Crew, E.; Yan, H.; Shan, S.; Skeete, Z.; Mott, D.; Krentsel, T.; Yin, J.; Chernova, N.; Luo, J.; et al. Bifunctional Nanoparticles for SERS Monitoring and Magnetic Intervention of Assembly and Enzyme Cutting of DNAs. J. Mater. Chem. B 2013, 1, 4320-4330.
- (9) Li, J.; Skeete, Z.; Shan, S.; Yan, S.; Kurzatkowska, K.; Zhao, W.; Ngo, Q. M.; Holubovska, P.; Luo, J.; Hepel, M.; et al. Surface Enhanced Raman Scattering Detection of Cancer Biomarkers with Bifunctional Nanocomposite Probes. Anal. Chem. 2015, 87, 10698-
- (10) Wang, L.; Luo, J.; Shan, S.; Crew, E.; Yin, J.; Zhong, C. J.; Wallek, B.; Wong, S. S. S. Bacterial Inactivation using Silver-Coated Magnetic Nanoparticles as Functional Antimicrobial Agents. Anal. Chem. 2011, 83, 8688-8695.

- (11) Lim, D.-K.; Jeon, K.-S.; Kim, H. M.; Nam, J.-M.; Suh, Y. D. Nanogap-Engineerable Raman-active Nanodumbbells for Single-Molecule Detection. *Nat. Mater.* **2010**, *9*, 60–67.
- (12) Skeete, Z.; Cheng, H.-W.; Ngo, Q. M.; Salazar, C.; Sun, W.; Luo, J.; Zhong, C. J. Squeezed" Interparticle Properties for Plasmonic Coupling and SERS Characteristics of Duplex DNA Conjugated/Linked Gold Nanoparticles of Homo/Hetero-Sizes. *Nanotechnology* **2016**, *27* (32), 325706.
- (13) Lee, J. H.; Nam, J. M.; Jeon, K. S.; Lim, D. K.; Kim, H.; Kwon, S.; Lee, H.; Suh, Y. D. Tuning and Maximizing the Single-Molecule Surface-Enhanced Raman Scattering from DNA-Tethered Nanodumbbells. *ACS Nano* **2012**, *6*, 9574–9584.
- (14) Lee, H. M.; Lee, J.-H.; Kim, H. M.; Jin, S. M.; Park, H. S.; Nam, J.-M.; Suh, Y. D. High-precision Measurement-Based Correlation Studies among Atomic Force Microscopy, Rayleigh Scattering, and Surface-Enhanced Raman Scattering at the Single-Molecule Level. *Phys. Chem. Chem. Phys.* **2013**, *15*, 4243–4249.
- (15) Ci, X.-T.; Wu, B.-T.; Song, M.; Chen, G.-X.; Liu, Y.; Wu, E.; Zeng, H.-P. Deep-Ultraviolet Surface Plasmon Resonance of Al and Al_{core} /Al₂O_{3shell} Nanosphere Dimers for Surface-Enhanced Spectroscopy. *Chin. Phys. B* **2014**, 23 (9), 097303.
- (16) Lee, J. H.; You, M. H.; Kim, G. H.; Nam, J. M. Plasmonic Nanosnowmen with a Conductive Junction as Highly Tunable Nanoantenna Structures and Sensitive, Quantitative and Multiplexable Surface-Enhanced Raman Scattering Probes. *Nano Lett.* **2014**, *14*, 6217–6225.
- (17) Pileni, M. P. Inorganic Nanocrystals Self Ordered in 2D Superlattices: How Versatile are the Physical and Chemical Properties? *Phys. Chem. Chem. Phys.* **2010**, *12*, 11821–11835.
- (18) Saikia, K.; Sen, D.; Mazumder, S.; Deb, P. Reassembling Nanometric Magnetic Subunits into Secondary Nanostructures with Controlled Interparticle Spacing. *RSC Adv.* **2015**, *5*, 694–705.
- (19) Srivastava, S.; Samanta, B.; Jordan, B. J.; Hong, R.; Xiao, Q.; Tuominen, M. T.; Rotello, V. M. Integrated Magnetic Bionanocomposites through Nanoparticle-Mediated Assembly of Ferritin. *J. Am. Chem. Soc.* 2007, 129, 11776–11780.
- (20) Crew, E.; Yan, H.; Lin, L.; Yin, J.; Skeete, Z.; Kotlyar, T.; Tchah, N.; Lee, J.; Bellavia, M.; Goodshaw, I.; et al. DNA Assembly and Enzymatic Cutting in Solutions: A Gold Nanoparticle based SERS Detection Strategy. *Analyst* 2013, 138, 4941–4949.
- (21) Lim, I.-I. S.; Chandrachud, U.; Wang, L.; Gal, S.; Zhong, C. J. Assembly-disassembly of DNAs and Gold Nanoparticles: A Strategy of Intervention based on Oligonucleotides and Restriction Enzymes. *Anal. Chem.* **2008**, *80*, 6038–6044.
- (22) Nicewarner-Pena, S. R.; Freeman, R. G.; Reiss, B. D.; He, L.; Pena, D. J.; Walton, I. D.; Cromer, R.; Keating, C. D.; Natan, M. J. Submicrometer Metallic Barcodes. *Science* **2001**, *294*, 137–141.
- (23) Njoki, P. N.; Lim, I.-I. S.; Mott, D.; Park, H. Y.; Khan, B.; Mishra, S.; Sujakumar, R.; Luo, J.; Zhong, C. J. Size Correlation of Optical and Spectroscopic Properties for Gold Nanoparticles. *J. Phys. Chem. C* 2007, 111, 14664.
- (24) Njoki, P. N.; Luo, J.; Kamundi, J. M. M.; Lim, S.; Zhong, C. J. Aggregative Growth in the Size-Controlled Growth of Monodispersed Gold Nanoparticles. *Langmuir* **2010**, *26*, 13622–13629.
- (25) Hostetler, M. J.; Templeton, A. C.; Murray, R. W. Dynamics of Place-Exchange Reactions on Monolayer-Protected Gold Cluster Molecules. *Langmuir* 1999, 15, 3782–3789.
- (26) Cheng, H. W.; Li, J.; Wong, S.; Zhong, C. J. Assessment of Aggregative Growth of MnZn ferrite Nanoparticles. *Nanoscale* **2016**, *8*, 19359–19367.